X-ray Absorption and Magnetic Circular Dichroism in CVD Grown Carbon Nanotubes

Original
X-ray Absorption and Magnetic Circular Dichroism in CVD Grown Carbon Nanotubes / Bellucci, Stefano; Cataldo, Antonino; Tagliaferro, Alberto; Giorcelli, Mauro; Micciulla, Federico. - In: CONDENSED MATTER. - ISSN 2410-3896. - ELETTRONICO. - 12:(2019). [10.3390/ma12071073]

Publisher:
Antonio Bianconi

Published
DOI:10.3390/ma12071073

Published in Proc. AIAA Guidance, Navigation, and Control Conference, Boston, MA, August 19 - 22, 2013

The control challenges for the Next Generation Gravity Mission

Enrico Canuto[1], Andrés Molano-Jimenez[2]
Politecnico di Torino, Torino, 10129, Italy

A. Bacchetta, M. Buonocore, S. Cesare[3]
Thales Alenia Space Italia, Torino, Italy

and

B. Girouart, L. Massotti[4]
ESA-ESTEC, The Netherlands

The Next Generation Gravity Mission (NGGM) in preparation by the European Space Agency aims to monitor the temporal variations of the Earth gravity field using pair of satellites orbiting at low altitude, whose distance is precisely measured by laser interferometry. The design of the control system for these satellites is particularly challenging due to the performance requirements and the number of functions that must be accomplished in close coordination: orbit maintenance, formation keeping, attitude tracking and stabilization, drag compensation and laser beam pointing.

Nomenclature

k = satellite index, $k=1$ preceding, $k=2$ following.

$\vec{r}_k, \vec{r}$ = Earth-centered radius of the satellite k and of the formation centre of mass (CoM) C

$\vec{o}_1, \vec{o}_2, \vec{o}_3$ = axes of the formation local orbital frame (FLOF)

r_x, r_z = components of $\vec{r}$ in the FLOF frame

$d = |\Delta\vec{r}|$ = distance between the satellite CoMs, length of the satellite-to-satellite line (SSL)

Δd = overall distance variation between the centres of mass of the satellites

Δd_D = distance variation between the centres of mass of the satellites produced by drag forces

Δd_G = distance variation between the centres of mass of the satellites produced by gravity forces

$\vec{D}_k$ = non-gravitational (drag) acceleration of the satellite k .

$\vec{g}_k$ = gravitational acceleration of the satellite k

$\vec{g}_k$ = gravitational acceleration of the satellite k

$\vec{c}_{k1}, \vec{c}_{k2}, \vec{c}_{k3}$ = axes of the control frame of the satellite k

$\mathsf{q}_{ck}, \mathsf{q}_o, \mathsf{q}_k$ = quaternions of the control frame, of the FLOF and of the control frame in the FLOF

$\boldsymbol{\omega}_{ck}, \boldsymbol{\omega}_o, \boldsymbol{\omega}_k$ = angular rate vectors of the control frame, of the FLOF and of the control frame in the FLOF (in 'body' coordinates)

---

[1] Dipartimento di Automatica e Informatica, Corso Duca degli Abruzzi 24, 10129 Torino, Italy, enrico.canuto@polito.it, Senior Member.

[2] Dipartimento di Automatica e Informatica, Corso Duca degli Abruzzi 24, 10129 Torino, Italy.

[3] Thales Alenia Space Italia, Strada Antica di Collegno 253, 10146 Torino, Italy.

[4] ESA-ESTEC, Keplerlaan 1, 2200 AG Noordwijk ZH, The Netherlands.

$J_k, \mathbf{M}_k, \mathbf{M}_{dk}$ = inertia tensor, command torque and total disturbance torque (in 'body' coordinates)
F = scientific measurement band
$\boldsymbol{\theta}_k$ = Euler angle vector assuming small q_k
$q_{k,nom}, d_{nom}, r_{nom}, \boldsymbol{\omega}_{nom}, ...$ = nominal (reference) values of AOCS
$\Delta d_{nom} = d - d_{nom}, \Delta r_z = r_z - r_{nom}, \Delta \boldsymbol{\omega} = \boldsymbol{\omega}_o - \boldsymbol{\omega}_{nom}, ...$ = perturbations, tracking errors
ω_o, P_o = mean orbit angular rate and period
$\mathbf{a}_k, \mathbf{a}$ = residual non gravitational acceleration, generic residual
$\mathbf{F}_k, \mathbf{D}_k, m_k = m$ = command force, non-gravitational disturbance (drag and thruster noise), mass
$\Delta \mathbf{x}_k$ = state vector of the FLOF perturbation dynamics, including radius and distance perturbations and their rates (6 variables), angular rate perturbations and their integrals (6 variables).
$\mathbf{x}_a, \mathbf{a}_d, \mathbf{s}_d$ = state variables of the thruster to accelerometer dynamics and of the disturbance dynamics (linear and angular)
$\mathbf{y}_a, \mathbf{e}_a$ = accelerometer measurement and model error
$\mathbf{d}, \mathbf{d}_t, \mathbf{d}_a$ = total disturbance recovered by the embedded model, sum of the disturbance to be rejected and of accelerometer drift
$\mathbf{w}, \mathbf{w}_x$ = total white noise and generic component
$\mathbf{p}$ = state of the noise estimator dynamics (if necessary)
$\mathbf{u}, \mathbf{u}_{ref}$ = total command including drag-free and reference command (attitude and formation)

I. Introduction

Following the success of the Earth gravity missions GRACE (http://www.nasa.gov/mission_pages/Grace/) and GOCE (http://www.esa.int/Our_Activities/Observing_the_Earth/GOCE), the scientific communities and the space agencies have started to focus their attention and effort towards the preparation of their successors. In particular, since 2003 the European Space Agency (ESA) has promoted studies to establish the scientific requirements, to identify the most appropriate measurement techniques, to start the associated technology developments, and to define the system scenarios for a "Next Generation Gravity Mission" (NGGM, Ref. 1 2). The objective established by the scientific communities for the NGGM consists in measuring the temporal variations of the Earth gravity field over a long time span (possibly covering a complete solar cycle) with high spatial resolution (comparable to that provided by GOCE) and high temporal resolution (weekly or better, Ref. 3). The products of such a mission will allow investigating with unprecedented details geophysical phenomena involving re-distribution and transportation of the Earth mass in the atmosphere, continental hydrosphere, oceans, cryosphere, and lithosphere, and will find wide application in geodesy, geophysics, hydrology, ocean circulation and many other disciplines.

The most appropriate measurement technique identified for such mission is the "Low-Low Satellite-Satellite Tracking" in which two satellites flying in loose formation in a low Earth orbit act as proof masses immersed in the Earth gravity field. The distance variation between the satellites and the non-gravitational accelerations of the satellites, measured respectively by a laser interferometer (with sub-micrometric resolution) and by ultra-sensitive accelerometers (like those installed on GOCE), are the fundamental observables from which the Earth gravitational field is obtained. Suitable satellite formations for this mission include the "In-line" (the simplest one), the "Pendulum" (more complex but also scientifically more fruitful) and the "Bender-type" (Ref. 4) constellation (providing the best scientific performance, but requiring two satellite pairs on different orbital planes), with an inter-satellite distance in the range ~100-200 km. Circular orbits with altitudes in the range 300-400 km and polar inclination (except for the second pair of the Bender formation which must fly at a medium inclination) are suitable for the NGGM, providing all-latitude coverage, short repeat cycles/sub-cycles and a still excellent gravity signal compatibly with a long lifetime. Each satellite shall be designed for a long mission lifetime in low-Earth-orbit, large variation of the solar illumination, minimum disturbance to the payload and shall be endowed with a complex control system capable of accomplishing several tasks in close coordination: orbit maintenance, formation keeping, attitude stabilisation, drag compensation and laser beam pointing at micro-radian level.

This paper presents an overview of the NGGM mission defined by Thales Alenia Space Italia (TAS-I) within the preparatory studies and technology development projects carried out for the European Space Agency (ESA), focusing in particular on the preliminary design of the control system, performed in cooperation with Politecnico di Torino.

II. NGGM Overview

A. Low-Low Satellite-Satellite Tracking principle

The principle of the Low-Low Satellite-Satellite Tracking (LL-SST) technique is illustrated in Fig 1.

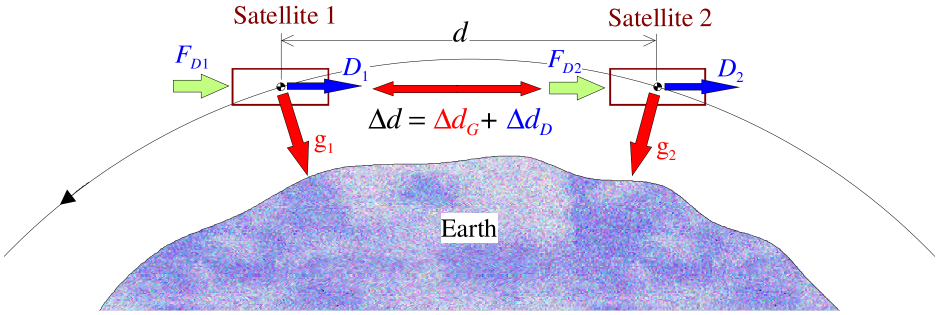

Fig 1. Principle of the LL-SST technique for measuring Earth's gravity field.

It makes use of a pair of satellites $k = 1, 2$ flying in loose formation at low altitude. The information about the Earth gravity field is provided by the distance variation between the centres of mass (COMs) of the two satellites (Δd_G) produced by the gravity acceleration $\vec{g}_k$. In general the satellite orbital motion (especially at low altitudes) is perturbed by both gravitational and non-gravitational accelerations: the contribution the latter must be identified and separated in order to single out the purely gravitational effect. Thus, Δd_G is formally obtained as:

$$\varDelta d_G = \varDelta d - \varDelta d_D \tag{1}$$

where:

1) Δd is the total distance variation between the COMs, whatever the source,
2) Δd_D is the distance variation produced by non-gravitational (i.e. drag) acceleration $\vec{D}_k$ of the satellites along the line joining the COMs.

The fundamental observables of the LL-SST are therefore: Δd (measured by a distance metrology), $\vec{D}_k$ (measured by accelerometers).

B. Operational orbit

The operational orbit must be nominally circular so that, flying at a nearly constant altitudes, the satellites are subject to a homogeneous mean gravity signal strength along the trajectory. From a scientific standpoint, the orbit altitude must be as low as possible to increase the measurement sensitivity, particularly to small scale gravity field variations. On the other hand, the requirement of a long mission lifetime (covering a complete solar cycle) and the limited on-board resources put a constraint to the minimum altitude. Depending on the satellite configuration and on the type of formation, practical orbit altitudes fall in the range 300-400 km.

A high spatial resolution in the gravity field solutions calls for a uniform and dense coverage of the Earth surface, while a high temporal resolution requires to complete a fairly uniform coverage (sufficient to obtain a gravity field solution at medium-long wavelengths) in a relatively short time. A good compromise between these two exigencies is provided by orbits with main repeat cycle of about 1 month and sub-cycles of 1 week or less. The rapidity and density of the ground coverage are by far improved adding a second satellite pair, to the benefit of the reduction of the temporal aliasing errors in the gravity field solutions.

A near polar orbit (inclination = 90°±1°), is required in order to avoid gaps around the poles in the geographic coverage, which are undesirable for the study of the ice mass variation in the Arctic and Antarctic regions. In the 2-satellite-pairs, "Bender-type" constellation (illustrated in Fig 2), the optimal inclination of the second pair is between 63° (Ref. 4) and 72° (Ref. 5), depending on the application.

C. Satellite formations

Among the possible geometries of a 2-satellite formation, two are considered suitable and viable for the implementation of the NGGM: “pearl string” (or “in-line”) and the “pendulum” formations.

In the pearl-string formation the two satellites fly on the same orbit, with different true anomalies ($\Delta\nu$), as illustrated in Fig 2. The in-line formation samples the gravity field in the along-track direction only. On a polar orbit, this formation is more sensitive to North-South variations of the gravitational field (and mass transport) than to East-West variations, which is reflected in an-isotropic signal structures leading to the well-known North-South striations in the GRACE solutions (Ref. 6). On the other hand, the in-line formation leads to the simplest satellite and payload configuration, since the satellite exposes always the same cross section to the main component of the drag, it keeps a constant Earth-pointing attitude and the satellite-to-satellite distance changes very slowly and by a small amount around a constant mean value.

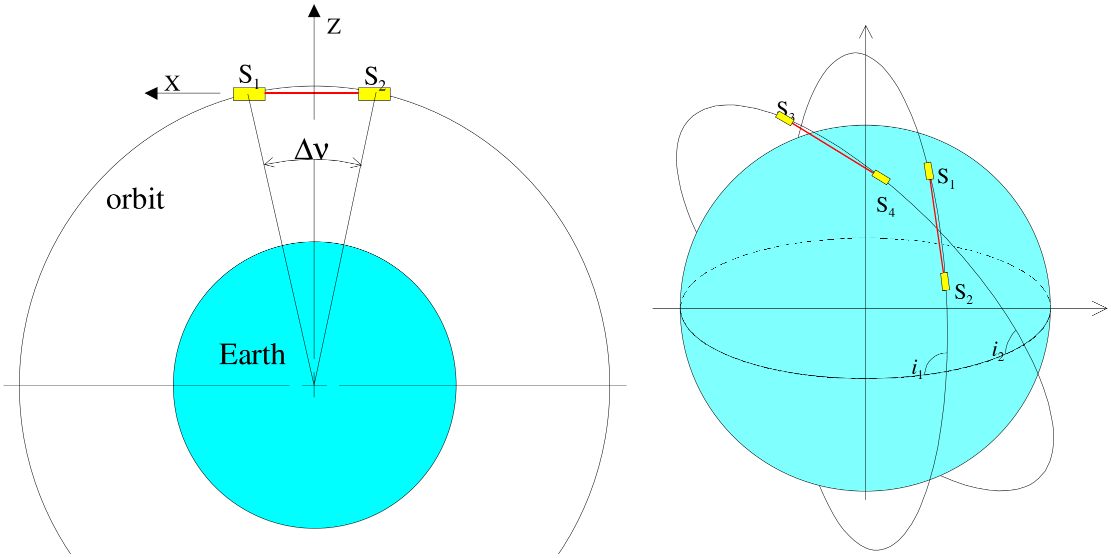

Fig 2. **Pearl-string formation geometry (left). Two pearl-string formations in “Bender-type” constellation (right).**

In the pendulum formation the two satellites fly on intersecting orbits, with different inclinations or longitudes of ascending nodes (Fig 3). From a scientific point of view a pendulum obtained with different ascending nodes is superior to that obtained with different inclinations. In fact, stripes occur mainly in the lower latitudes caused by North-South observations. With different inclinations the cross-track observations occur at the higher latitudes and stripes would still appear. The pendulum formation mainly captures cross-track and along-track gravity signals. Here the satellite is again nominally Earth pointing, but must perform a periodic yaw-steering manoeuvre (with angular amplitude $\alpha_{\max}$, and frequency = orbit frequency) for maintaining the alignment of the metrology laser beam to the satellite-satellite line. Consequently the main component of the drag force sweeps a large angular sector around the satellite and the satellite-to-satellite distance experiences much larger oscillations than in the pearl-string formation, with a significant Doppler shift on the frequency of the metrology laser beam travelling between the satellites. Therefore, although the maximum scientific return is obtained for a pendulum aperture angle $\alpha_{\max} = 45°$, for a practical implementation $\alpha_{\max}$ must be limited in the range 10°-20°, with a nominal reference value of 15°.

In both formation types, an inter-satellite distance d in the range ~100-200 km is compatible with both the scientific objectives and the practical implementation of the mission.

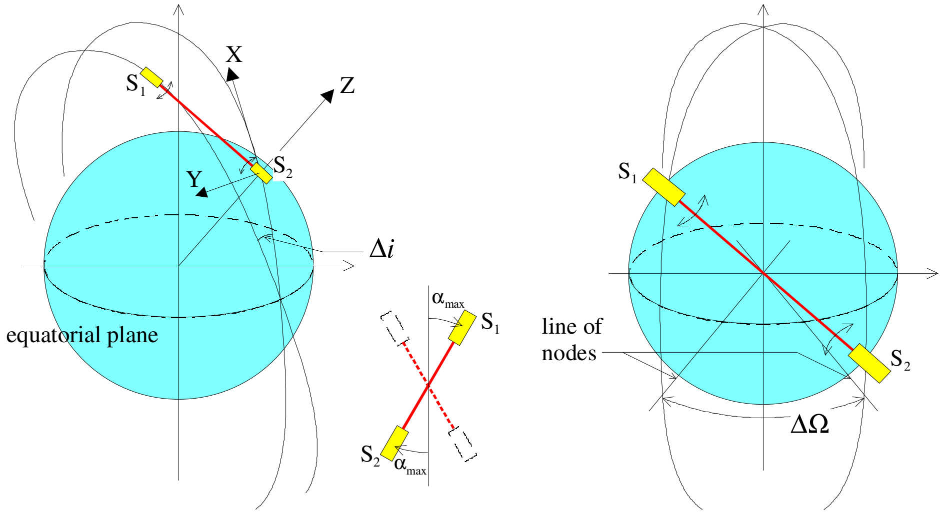

Fig 3. Pendulum formation with separation in inclination (left) and with separation in longitudes of ascending nodes (right).

D. Payload overview

The complete set of instruments involved in the measurement of the fundamental observables of the NGGM includes (see Fig. 4).

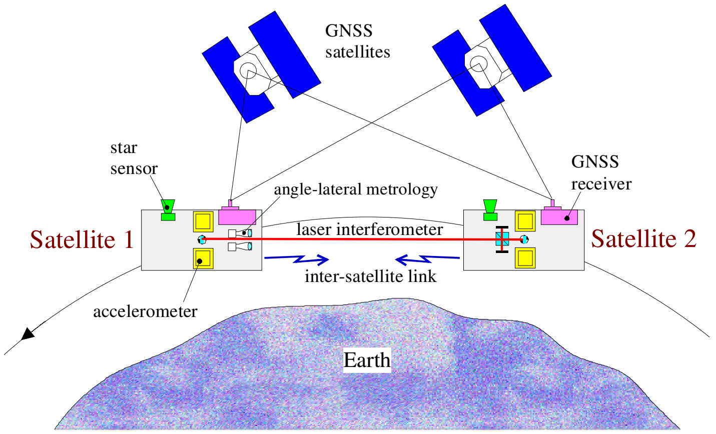

Fig 4. Instruments involved in the measurement of the LL-SST fundamental observables.

1) A laser interferometer, which provides the distance variation between two retro-reflectors installed ideally in the COMs of the two satellites.
2) An accelerometer set, which provides the non-gravitational linear acceleration of the COM of each satellite.
3) An auxiliary metrology, which provides the Satellite 1 angular orientation and lateral displacements relative to the laser beam emitted by Satellite 2 (information needed for the acquisition of the optical link between the satellites and for processing the distance and acceleration measurements).
4) A Global Navigation Satellite System (GNSS) receiver, which provides the absolute and relative position of the satellites.
5) Star sensors, which provide the inertial attitude of the satellites.

The core of the satellite-satellite distance variation measurement system devised by TAS-I is a Michelson-type heterodyne laser interferometer based on the retro-reflector scheme (laser transmitted by Satellite 2 and back-reflected by Satellite 1) and adapted for the long-distance operation (Ref. 7). The scheme of the interferometer and its configuration are shown in Fig. 5. The retro-reflectors constituting the optical references for the distance variation measurement shall be nominally collocated in the COMs of the two satellites. The metrology scheme based on the retro-reflection of the laser beam is suitable up to an inter-satellite distance of 100 km. Above this distance, the “optical transponder” scheme (the laser beam transmitted by Satellite 2 is “regenerated” by a second laser source in Satellite 1 before being retransmitted) must be adopted (Ref. 8).

The angular orientation/lateral displacement metrology consists of three small telescopes which pick up portions of the laser beam received by Satellite 2 and measure position and intensity on the light spots focused on the detectors (Ref. 9).

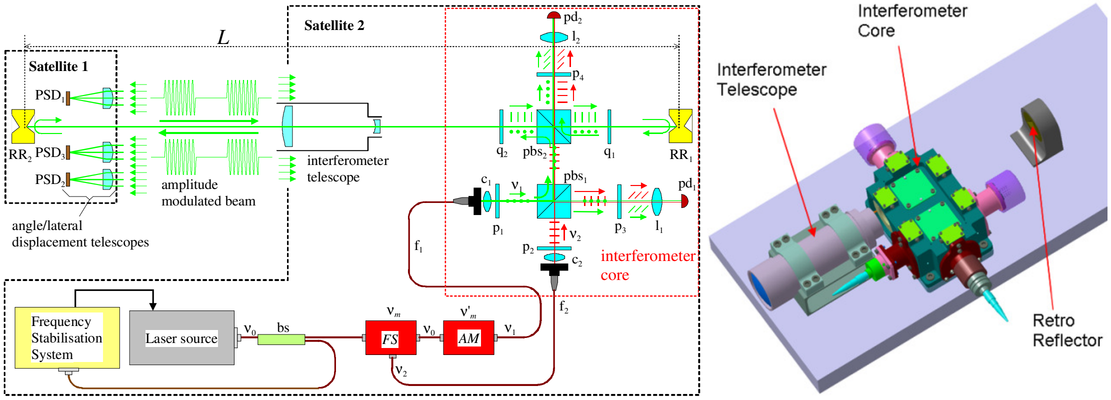

Fig 5. **Functional scheme and configuration of the on-board interferometer.**

The non-gravitational acceleration of the satellite COM is measured by a set of accelerometers like those used on GOCE (Ref. 10), endowed with two ultra-sensitive axes an one less sensitive axis (for ground testing). A set of four accelerometers arranged around the optical bench of the laser interferometer as shown in Fig 6 measures the linear and angular accelerations about each satellite axis, and in particular in the direction of the laser beam, with the maximum accuracy. The intersection of the baselines between the two accelerometer pairs is nominally collocated in the satellite COM.

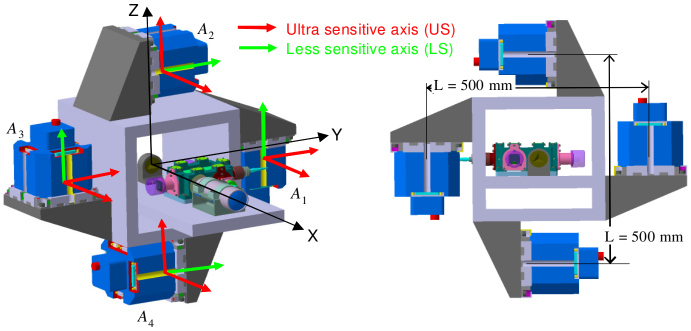

Fig 6. **Arrangement of four accelerometers for measuring the non-gravitational accelerations.**

A two-accelerometer configuration, requiring less space and resources for its accommodation on the satellite, has been also defined (see Fig 7); the linear and angular acceleration measurement performance is obviously poorer, but still compatible with the mission objectives.

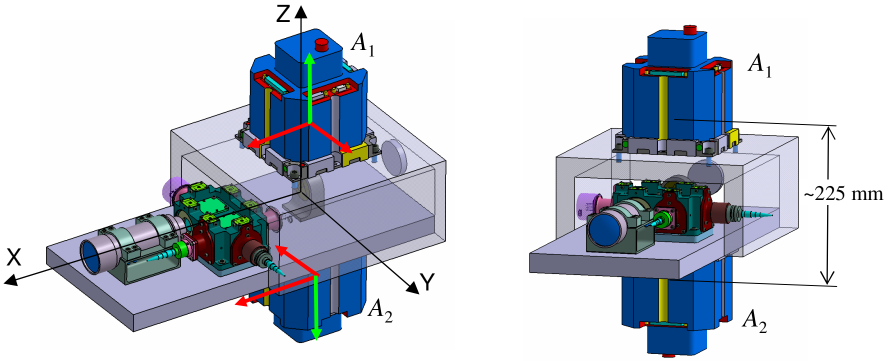

Fig 7. Arrangement of two accelerometers for measuring the non-gravitational accelerations.

E. Satellite configuration overview

The satellite configuration defined by TAS-I is based on a customized version of the platform which is used for the Iridium-Next constellation (Fig. 8). The configuration and the total mass are such that two satellites can be launched together with Dnepr or Vega.

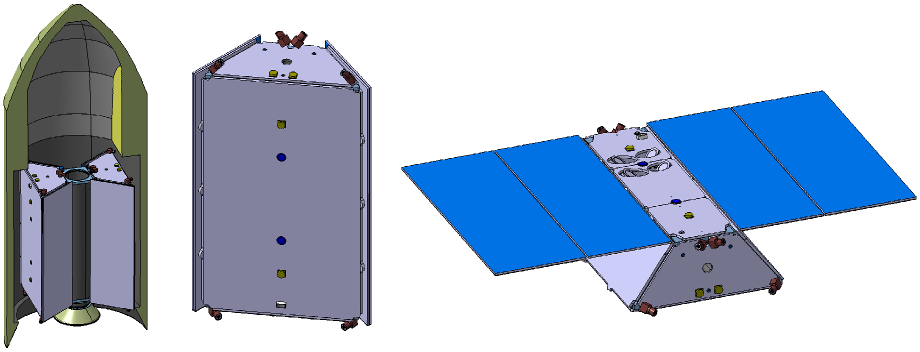

Fig 8. Satellite launch configuration inside Dnepr (left) and on-orbit configuration (right).

The optical bench with the interferometer core surrounded by the accelerometers is collocated in the middle of satellite. A central slightly flared tube lets the laser beams in and out as needed by the interferometer.

The solar array consists of two wings (with 2 panels each) hinged on the top side of the satellite (opposite to the Earth) and deployed on orbit. No mechanisms are employed for the orienting the solar panels during the mission, to avoid sources of micro-vibrations. Since the operational orbit is not Sun-synchronous, the satellite performs a periodic roll maneuver (e.g. once per month, a continuous smooth roll maneuver is also possible) for keeping a suitable exposure of the panels to the sunlight (Fig. 9).

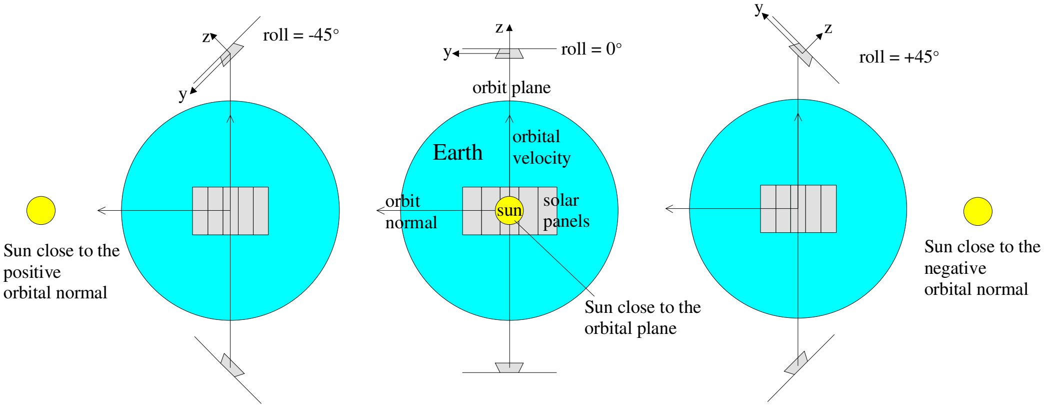

Fig 9. Satellite orientations for ensuring the proper illumination of the solar panels.

Four star trackers pointing in different directions are employed to ensure the inertial attitude measurement availability for any nominal illumination condition from the Sun, Earth and Moon along the mission. Attitude acquisition and safe modes are managed by means of coarse Earth and Sun sensors.

Eight electric thrusters are mounted on the front side (facing the satellite motion) and the rear side of the satellite. The thrusters are oriented in such a way to enable the application of forces and torque about all axes, with a prevalent component along the orbital velocity. The attitude control function of the thrusters is complemented by three magnetic torquer bars.

III. Control Requirements

A. Functional requirements

The Attitude and Orbit Control System (AOCS) for the NGGM must accomplish the following functions.

1) *Orbit altitude control*. The mean orbit altitude is subject to decay due to non-gravitational accelerations during the early phases and the residual accelerations of the drag-free control during the science phase. Therefore must be constantly monitored and maintained around the nominal value. The control range must enable to keep the selected repeat cycle.

2) *Satellite formation control*. No stringent requirements apply to the two-satellite formation control. In fact, since in the LL-SST techniques the satellites themselves act as proof masses, they should be nominally free to move under the action of the gravity field. In practice, the orbital perturbations of non-gravitational nature (mainly due to residual accelerometer bias and drift during the science phase), if not compensated, drive the satellites away from the initial formation geometry with consequences on the gravity field sampling (e.g. due to the modification of the satellite-to-satellite baseline or of the maximum aperture angle of the pendulum) and of the measurements (e.g. the satellite-to-satellite distance can exceed the working range of the laser interferometer). Thus, the satellite formation must be kept bounded around the initial parameters through a “weak” control action that must not interfere with the scientific measurements (“loose formation” concept), by operating on bandwidth separate from the measurement one.

3) *Non-gravitational acceleration control (drag-free control)*, necessary to reduce the non-gravitational acceleration background of each satellite at a level, below the accelerometer saturation threshold, where the measurement errors arising from the coupling of the accelerometer imperfections with the residual acceleration are compatible with the mission performance. The non-gravitational acceleration control must be coordinated with the orbit and formation control, to avoid that the forces applied to the satellite for maintaining the operational altitude and the formation geometry are compensated by the drag control action.

4) *Satellite-to-satellite line pointing control*, necessary for aligning the beam of the laser interferometer to the satellite-to-satellite line, and to maintain this alignment within the requested bounds. This function is totally attributed to the satellite attitude control system, without employing a laser beam pointing mechanism for avoiding sources of micro-vibrations. The satellite attitude around the satellite-satellite line (roll angle), driven by the illumination of the solar panels, is not subject to stringent control requirements. SSL pointing is the main attitude task during the science phase, but it must preceded by a careful alignment of the body frame to the formation frame, which is a prerequisite for performing the acquisition of laser beams by the optical metrology and the subsequent alignment.

Orbit and formation control, though assigned with different requirements, are strictly interacting, because of the coupling between radial and tangential orbital perturbations, as it is expressed by Hill’s equations. Thus control design has been tackled as a unique formation control problem, whose target is to keep constant the mean distances of the triangle edges which is formed by the formation satellites and the Earth CoM. Notwithstanding the ‘loose’ formation requirements, formation control design must be kept as challenging because of the very limited thrust (a few millinewton) which is left by drag-free and attitude control, and the bandwidth limit imposed by the drag-free control.

B. Performance requirements

The main performance requirements for the AOCS functions described in the previous paragraph are provided in Table 1. Particularly tight are the requirements on the drag-free control (although this performance has been already demonstrated on-orbit by GOCE, along a single axis), and on the laser beam pointing precision and stability in operational conditions. For the optical link acquisition, a pointing precision of 10^{-4} rad (far-field divergence of the laser beam) is sufficient.

Table 1. Main performance requirements for the AOCS.

No	Control object	Requirement	Remarks
1	Mean orbit altitude h	$h = h_{\text{reference}} \pm 100$ m	Based on the repeat cycle control
2	Satellite-satellite distance d	$d = d_{\max} +0\% \div -10\%$	For all formations
3	Maximum aperture angle $\alpha_{\max}$	$10° \le \alpha_{\max} \le 20°$	For pendulum formations.
4	Non-gravitational linear acceleration of COM along X,Y,Z	$\le 10^{-6}$ m/s^2 $\le 5 \cdot 10^{-9}$ m/s^2/√Hz in MBW (a)	(a) Scientific measurement band: between 1 mHz and 100 mHz
5	Satellite pointing along the satellite-satellite line in operational conditions.	$\le 2 \cdot 10^{-5}$ rad	Pointing precision of the metrology laser beam emitted by the satellite towards the opposite satellite.
6	Satellite pointing stability along the satellite-satellite line.	$\le 10^{-6}$ rad/√Hz	Constraint on the jitter of the metrology laser beam emitted by the satellite.
7	Satellite rotation around the satellite-to-satellite line.	≤ 2 mrad	Constraint on the satellite roll motion.

IV. Control System Preliminary Design and Performance Assessment

A. Control frames

The main AOCS mode is the Science Mode (SCM), which is demanded to meet the performance requirements in Table 1. Here we focus on this mode. Control design requires the following frames definition and materialization.

The key formation frame is the so-called FLOF (Fig 10) $\mathsf{O} = \{C, \vec{o}_1, \vec{o}_2, \vec{o}_3\}$ whose first axis $\vec{o}_1$ is the satellite-to-satellite line aligned with the relative CoM position $\Delta\vec{r} = \vec{r}_1 - \vec{r}_2$. The second axis $\vec{o}_2$ is orthogonal to the formation plane defined by $\{\Delta\vec{r}, \vec{r} = (\vec{r}_1 + \vec{r}_2)/2\}$, $\vec{r}$ being the radius of the formation CoM C. Formally

$$\begin{aligned} &\vec{o}_1 = \frac{\Delta\vec{r}}{d},\ \vec{o}_2 = \frac{\vec{r}/r \times \Delta\vec{r}/d}{\left|\vec{r}/r \times \Delta\vec{r}/d\right|},\ \vec{o}_3 = \frac{\vec{r}}{r},\ d = \left|\Delta\vec{r}\right|,\ r = \left|\vec{r}\right|, \\ &\vec{r} = r_x\vec{o}_1 + r_z\vec{o}_3 \end{aligned} \tag{2}$$

where $\vec{r}$ has been decomposed into longitudinal and radial components.

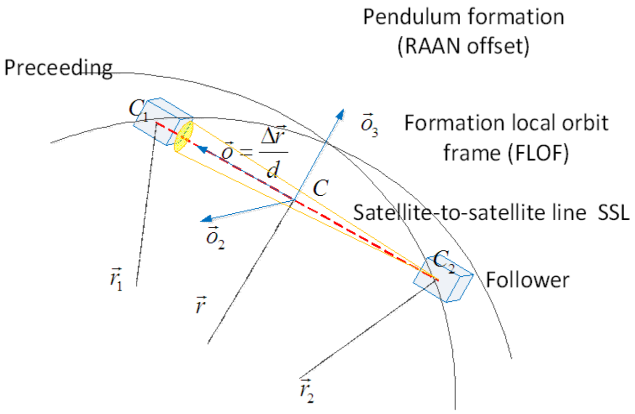

Fig 10. **Formation local reference frame (FLOF).**

The FLOF is materialized by the GNSS range measurements as soon as GNSS receivers become operational. During the science phase, the first FLOF axis $\vec{o}_1$ is materialized by the laser beam lunched by each satellite and received by the optical metrology on the companion satellite (see Section II.D). The first axis $\vec{c}_{k1}$ of the attitude control frame $\mathcal{C}_k=\{C_k,\vec{c}_{k1},\vec{c}_{k2},\vec{c}_{k3}\}$ is defined by the optical metrology, and specifically by the axis $\vec{s}_k$ of the most accurate sensor under operation, in the motion direction. The second axis is close to the axis $\vec{a}_k$ of the accelerometer pair. Formally

$$\vec{c}_{k1}=\vec{s}_k,\ \vec{c}_{k2}=\frac{\vec{a}_k-\vec{s}_k\cdot\vec{a}_k\vec{s}_k}{\left|\vec{a}_k-\vec{s}_k\cdot\vec{a}_k\vec{s}_k\right|},\ \vec{c}_{k3}=\vec{c}_{k1}\times\vec{c}_{k2}. \tag{3}$$

The optical materialization of the SSL and the control frame are illustrated in Fig 11. The SSL equation of the laser beam $\vec{b}_2$ launched by the satellite 2 holds

$$\begin{aligned}&\Delta\vec{r}_m=\overrightarrow{C_1C_2}-\overrightarrow{C_2L_2}-\overrightarrow{S_1C_1}\\&\left|\Delta\vec{r}_m\right|\le d\left(1+\frac{\left|\overrightarrow{C_2L_2}\right|+\left|\overrightarrow{S_1C_1}\right|}{d}\right)=d\left(1+\partial d_m\right)\end{aligned}, \tag{4}$$

and is affected by the segments $\overrightarrow{C_2L_2}$, $\overrightarrow{S_1C_1}$ (optical offset). Imposing $\partial d_m<1\ \mu\text{rad}$ in agreement with Table 1, row 6, and assuming $d\ge 100\ \text{km}$, the total optical offset should be less than 0.1 m. Since the offset, if partially known, may be treated by control algorithms as a known bias, the optical materialization of the SSL is fully compliant with pointing requirements.

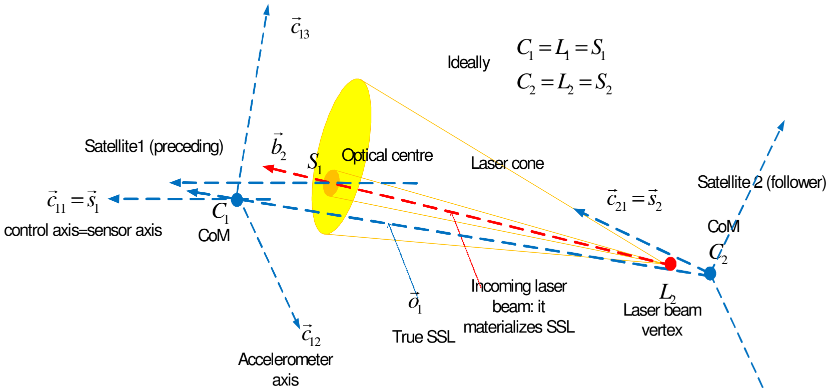

Fig 11. **Control frames and the optical materialization of the SSL.**

The optical metrology of the satellite k measures the 2D tilt (pitch and yaw) of the incoming laser beam $\vec{b}_j$ launched by the companion satellite j from the sensor axis $\vec{s}_k$. Optical metrology errors (bias and random errors) must be compatible with pointing requirements in Table 1. Different metrological configurations are possible, depending whether the laser beam is launched by a single satellite or by both. Here we assume that each satellite is equipped with a virtual sensor receiving a virtual laser beam. For instance the lateral optical metrology mentioned in Section II.D allows a single laser beam, but it must be equipped with a satellite interlink for transmitting the pointing error to the companion satellite which is launching the beam, but is free of optical metrology.

Each spacecraft is rotating around $\vec{c}_{k1}$ to expose solar panels to sun (Section II.E), but the control frame does not include such a rotation. In this way, attitude can be described by the vector $\boldsymbol{\theta}_k$ of small 3-2-1 Euler angles $\{\varphi_k, \theta_k, \psi_k\}$ between FLOF and control frame. Formally, by denoting FLOF and control frame quaternions with q_o and q_{ck}, the attitude quaternion reads as

$$\mathsf{q}_k = \mathsf{q}_o^{-1} \otimes \mathsf{q}_{ck} \cong q_{k0} \begin{bmatrix} 1 \\ \boldsymbol{\theta}_k / 2 \end{bmatrix}. \tag{5}$$

The control frame must not be confused with the body frame B, which is fully rotating with the spacecraft. Body-to-control transformation includes the nominal roll φ_{nom} and a 3-2-1 partly known small rotation.

B. Embedded model and control objectives

AOCS is designed around a model of the spacecraft and formation dynamics to be included in the control algorithms (embedded model). The model is discrete time, but here for the sake of simplicity continuous time is used. Control requirements in Section III are formulated through reference values (or time profiles) of the model variables, corrupted by a tracking error. Error fluctuation is bounded as in Table I in terms of an absolute maximum value and in terms of a spectral density bound within the scientific measurement band

$$F = \{0.001 \le f \le 0.1 \text{ Hz}\}. \tag{6}$$

Attitude dynamics in terms of q_k and of the rate $\boldsymbol{\omega}_k$ is the following

$$\begin{aligned} \dot{\mathsf{q}}_k &= \frac{1}{2}\mathsf{q}_k \otimes \boldsymbol{\omega}_k \\ \dot{\boldsymbol{\omega}}_k &= \dot{\boldsymbol{\omega}}_{ck} + \mathbf{h}(\boldsymbol{\omega}_k, \boldsymbol{\omega}_o, \mathsf{q}_k), \\ \dot{\boldsymbol{\omega}}_{ck} &= J_k^{-1}\mathbf{M}_k + J_k^{-1}\mathbf{M}_{dk} \end{aligned} \tag{7}$$

where $\boldsymbol{\omega}_{ck}$ is the control frame angular rate, $\boldsymbol{\omega}_o$ is the FLOF angular rate, J_k is the inertia tensor, $\mathbf{M}_k$ is the command torque, $\mathbf{M}_{dk}$ is the total environment torque (disturbance) including gravity-gradient and gyro torques. Finally $\mathbf{h}$ accounts for the FLOF rotating axes. The ideal requirements (attitude and drag-free) are expressed as

$$\begin{aligned} \mathsf{q}_k &= \begin{bmatrix} 1 \\ \mathbf{q}_{k,nom} = \mathbf{0} \end{bmatrix} = \mathsf{q}_{k,nom} \\ \dot{\boldsymbol{\omega}}_{ck} &= J^{-1}\mathbf{M}_k + J^{-1}\mathbf{M}_{dk} = 0 \end{aligned} . \tag{8}$$

The former equality expresses perfect alignment of control frame and FLOF, the latter is the angular drag-free requirement. During science phase, the most challenging requirements concern the alignment of the laser beam with the SSL, formally of $\vec{c}_{k1}$ with $\vec{o}_1$ .The target misalignment is of the order of microradians within F. The relevant attitude control has been referred to as pointing control, and concerns the second and third components of $\boldsymbol{\theta}_k$ in (5) (pitch and yaw). The first component, roll, may fluctuate of milliradians. Outside the science mode, in order to recover a large deviation within a limited thruster authority, a smooth reference profile $\mathsf{q}_{k,nom}(t)$ might be the case. Drag-free requirement, which is restrictive within F, must be progressively relaxed below F to accommodate the attitude control authority. Dually, attitude control must respect the restrictive drag-free bound within F. This implies a strict frequency coordination between drag-free and attitude control.

Formation/orbit dynamics can be expressed in terms of the perturbations of a nominal formation subject to spherical gravity, having zero eccentricity, and defined by nominal distance, radius and angular rate as follows

$$d_{nom},\ r_{x,nom}=0,\ r_{z,nom}=r_{nom},\ \boldsymbol{\omega}^T_{nom}=\left[\omega_{x,nom}=0\quad \omega_{y,nom}=\omega_o\quad \omega_{z,nom}=0\right]. \tag{9}$$

In the pendulum formation of Fig 3, all the non-zero nominal variables in (9), except r_{nom}, are time-varying with the orbit period $P_o = 2\pi / \omega_o$, but they can be made constant by assuming that the nominal formation is pearl-string as in Fig 2. As such, pendulum oscillations become the free response of the perturbed equations. The six degrees-of-freedom perturbations can be split into

1) SSL length perturbation $\Delta d = d - d_{nom}$, and radius perturbations $r_x, \Delta r_z = r_z - r_{nom}$,
2) FLOF angular rate perturbations $\Delta\boldsymbol{\omega} = \boldsymbol{\omega}_o - \boldsymbol{\omega}_{nom}$.

Treating J2 and higher order harmonics as external disturbances, perturbed equations become linear and time-invariant like Hill's equations, they depend on the nominal parameters in (9), and are driven by residual non-gravitational acceleration $\mathbf{a}_k$ and gravity anomalies (including J2 and eccentricity) $\mathbf{g}_k$. The residual $\mathbf{a}_k$ is the sum of the command forces $\mathbf{F}_k$ and of the non-gravitational disturbances $\mathbf{D}_k$ (mainly drag). The compact form is

$$\begin{aligned}
&\Delta\dot{\mathbf{x}}(t) = A\left(\omega_o, d_{nom}, r_{nom}\right)\Delta\mathbf{x}(t) + \begin{bmatrix} B_1 & B_2 \end{bmatrix}\begin{bmatrix} \mathbf{a}_1 \\ \mathbf{a}_2 \end{bmatrix}(t) + \begin{bmatrix} G_1 & G_2 \end{bmatrix}\begin{bmatrix} \mathbf{g}_1 \\ \mathbf{g}_2 \end{bmatrix}(\Delta\mathbf{x}) \\
&\mathbf{a}_k(f) = \frac{1}{m}\left(\mathbf{F}_k + \mathbf{D}_k\right)
\end{aligned}, \tag{10}$$

where $\Delta\mathbf{x}$, sized $n_{\Delta x} = 12$, includes SSL length perturbations (and their rates) and FLOF angular rate perturbations (and their angles). $\mathbf{g}_k(\Delta\mathbf{x})$ is a periodic function. Only four perturbations need to be regulated to zero according to Table 1. They are the distance Δd, the radius components $r_x, \Delta r_z$ (replacing altitude variation) and the yaw rate ω_z (essential for the case of the pendulum formation):

$$\Delta d_{nom} = 0,\ r_{x,nom} = 0,\ \Delta r_{z,nom} = 0,\ \omega_{z,nom} = 0. \tag{11}$$

The CoM (or linear, as opposed to angular) drag-free requirement is to zero the residual accelerations, namely

$$\mathbf{a}_k = 0. \tag{12}$$

Like the angular drag-free, (12) is progressively relaxed outside F to accommodate the formation control authority. Dually, formation control must respect the restrictive drag-free bound within F, or otherwise said it should not perturb the 'nature', i.e. the formation free response of (10). This implies a strict frequency coordination between drag-free and formation control.

Each embedded model, (7) and (10), must be completed with a stochastic dynamics accounting for the disturbance class to be rejected, and specifically of $\mathbf{M}_{dk}$ in (7) and of $\mathbf{D}_k$ in (10). To be generic consider a disturbance acceleration $\mathbf{d}_t$ (either linear or angular) and a commanded acceleration $\mathbf{u}$ for each satellite k (the subscript has been dropped), which combine into the residual acceleration $\mathbf{a}$ as follows

$$\mathbf{a} = \mathbf{u} + \mathbf{d}. \tag{13}$$

On board accelerometers (see Section II.D) provide a measurement $\mathbf{y}_a$ which is related to $\mathbf{a}$ by a low-pass filter accounting for the chain from thruster to sensor, as follows

$$\begin{aligned}
&\dot{\mathbf{x}}_a(t) = A_a\mathbf{x}_a(t) + B_a\left(\mathbf{u}(t) + \mathbf{d}_t(t) + \mathbf{d}_a(t)\right) = A_a\mathbf{y}_a(t) + B_a\left(\mathbf{u}(t) + \mathbf{d}(t)\right) \\
&\mathbf{y}_a(t) = \mathbf{x}_a(t) + \mathbf{e}_a(t)
\end{aligned}, \tag{14}$$

where $\mathbf{d} = \mathbf{d}_t + \mathbf{d}_a$ is the total disturbance including accelerometer bias, drift and noise, and $\mathbf{e}_a$ is the model error encoding model discrepancies. Extensive studies during GOCE design (Ref. 13) pointed out the high-frequency spectral density of aerodynamic forces (up to 5 Hz) to be completed with thruster noise. A combination of white noise (thruster noise), first and second-order random drift (thruster noise and aerodynamic forces) is sufficient for recovering the class of the expected time realizations. It can be written as

$$\begin{aligned}&\begin{bmatrix}\dot{\mathbf{a}}_d\\ \dot{\mathbf{s}}_d\end{bmatrix}(t)=\begin{bmatrix}0 & I\\ 0 & 0\end{bmatrix}\begin{bmatrix}\mathbf{a}_d\\ \mathbf{s}_d\end{bmatrix}(t)+\begin{bmatrix}I & 0\\ 0 & I\end{bmatrix}\begin{bmatrix}\mathbf{w}_a\\ \mathbf{w}_s\end{bmatrix}(t),\ \begin{bmatrix}\mathbf{a}_d\\ \mathbf{s}_d\end{bmatrix}(0)=\begin{bmatrix}\mathbf{a}_{d0}\\ \mathbf{s}_{d0}\end{bmatrix}\\ &\mathbf{d}(t)=\begin{bmatrix}I & 0\end{bmatrix}\begin{bmatrix}\mathbf{a}_d\\ \mathbf{s}_d\end{bmatrix}(t)+\mathbf{w}_d(t)\end{aligned}, \tag{15}$$

upon definition of the arbitrary wide-band zero-mean bounded vectors (near to white noise, but without a modeled statistics, better defined in discrete-time) $\mathbf{w}_x, x=a,s,d$. Embedded Model Control has proved (Ref. 14) that their realization can be real-time retrieved from the accelerometer model error $\mathbf{e}_a$ up to a frequency band of about 0.5 Hz, which was sufficient for GOCE and is suitable to NGGM conditions. Retrieval occurs though a (static/dynamic) noise estimator (an all-pass filter), which under linear and time invariant assumption reads as

$$\begin{aligned}&\dot{\mathbf{p}}(t)=Q\mathbf{p}(t)+E\mathbf{e}_a(t),\ \mathbf{p}(0)=0\\ &\mathbf{w}(t)=M\mathbf{p}(t)+L\mathbf{e}_a(t)\end{aligned}, \tag{16}$$

where $\mathbf{w}$ is the complete noise vector. Stationary Kalman filter is a particular case of (16) with $Q=0,\ E=0,\ M=0$ and L depending on the noise statistics. The dynamic part in (16) becomes necessary when L is insufficient to guarantee closed–loop stability of the embedded model plus noise estimator (state predictor). This occurs when L is not completely free as for the attitude dynamics (Ref. 15), in which case the size of $\mathbf{p}$ is dictated by the constraints on L. No dynamics applies to the noise estimator of (15), since L is completely free as in Kalman filters. A stochastic dynamics similar to (15) applies to $\mathbf{M}_{dk}$ in (8).

One should be aware that $\mathbf{y}_a$ in (14) tends to be close to zero, because of drag-free control. Notwithstanding that, (15) and (16) allow to build up step by step, save and improve a careful time profile of the actual non gravitational forces and disturbance torques. GOCE drag-free performance in Fig 12 is the proof of that. The top segment in Fig 12 is the drag-free bound (PSD) in the scientific measurement band. Residuals vary at different epochs because of the variable solar activity that modifies thermosphere density.

The role of a disturbance model like (15) should become clear by writing the drag-free control law, which fixes the algorithm of $\mathbf{u}$ in (14). Since the thruster-to-accelerometer dynamics in (14) is asymptotical stable and wide-band (in the limit it approaches the Nyquist frequency of the accelerometer measurements, 5 Hz), the drag-free command is a pure combination of rejection and reference as follows

$$\mathbf{u}(t)=-\mathbf{a}_d(t)+\mathbf{u}_{ref}(t). \tag{17}$$

The former term in (17), in agreement with (15), tends to ideally zero $\mathbf{a}$ in (13), which is only possible within F, defined in (6), due to the accelerometer bias and drift. The latter term generically denotes formation and attitude commands in charge of counteracting the drag-free residuals and achieving the relevant targets. Of course $\mathbf{u}_{ref}$ must respect the drag-free targets and must constrain its authority to below F as shown in Fig 13 (what is achieved by hierarchical control and frequency coordination, see next section).

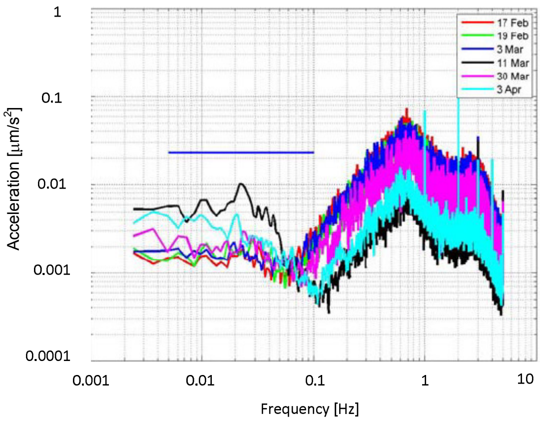

Fig 12. Experimental drag free residuals of the GOCE mission (along-track).

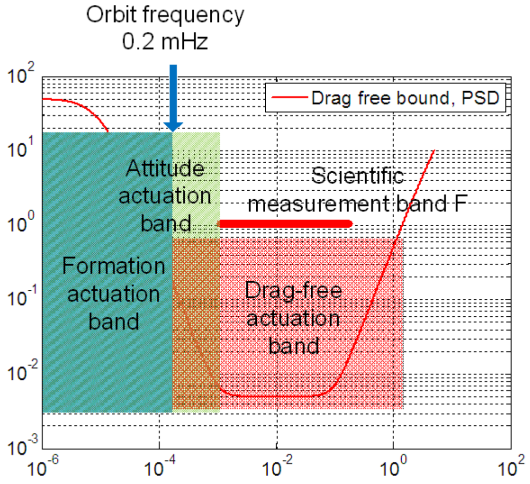

Fig 13. Frequency coordination of the inner and outer loops.

C. Control principles and architecture

The higher-level block-diagram of the AOCS during the science phase is in Fig 14. The principles behind it exploit the Embedded Model Control methodology (Ref. 11 , 12 , 13) and model decomposition.

1) Attitude and formation decoupling. By guaranteeing, since the early mission phases (as soon as thrusters, star trackers and GNSS become operational) milliradian alignment between control frame and FLOF, both frames can be confused. Thus the attitude quaternion q_k in (5), which is distributed to linear and angular drag-free blocks in Fig 14, can be approximated to be the nominal one in (8). Attitude and formation are further coupled in the thruster dispatching algorithm, because of the limited thrust (eight 2-mN thrusters are assumed as a baseline). Decoupling is obtained by ranking control functionalities: attitude and orbit control have the highest priority. Ranking works in two modes: some authorities are bounded, other ones may be temporarily cancelled thus degrading the control mode.
2) Hierarchical control. Attitude and formation/orbit control are split into inner and outer loops, to be frequency coordinated as mentioned above (see (17)). The inner loops (3 and 4 in Fig 14), which, because of the accelerometer bandwidth and accuracy, are wide-band (close to the Nyquist frequency of 5 Hz), create ideal channels from thrust to acceleration, which are disturbance-free and fast, both for formation and attitude control. However, to respect drag-free restrictions, such channels can only be employed by the outer loops (1 and 2, attitude and formation control) within a narrow band (<1 mHz), i.e. below the scientific frequency band F in (6) as Fig 13 shows.

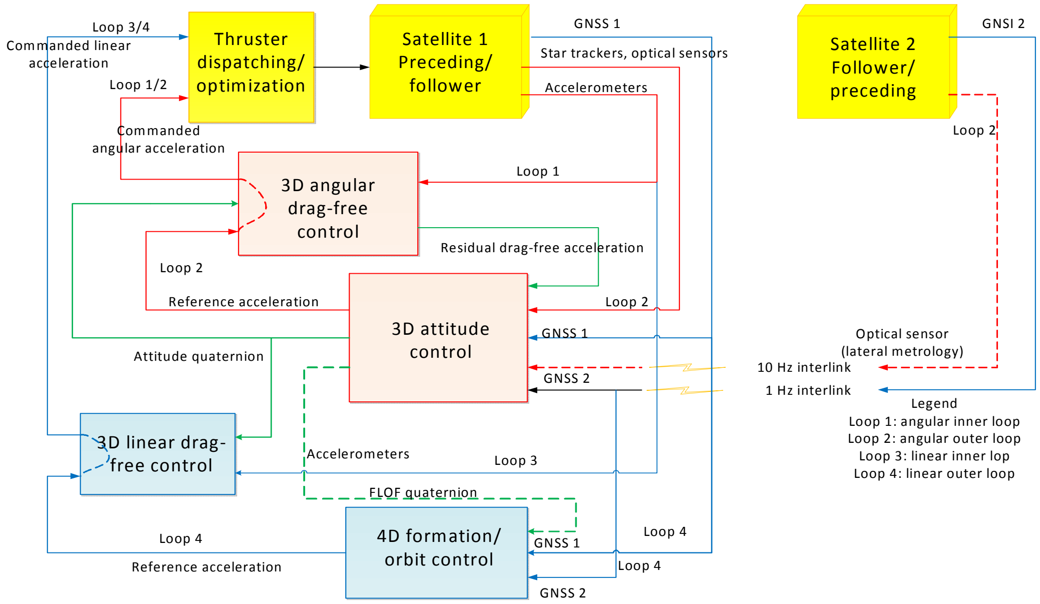

Fig 14. **Higher-level AOCS block-diagram (science mode)**

3) Coordinate decomposition applies to the four blocks in Fig 14 in a different manner. Drag-free control is decomposed into six independent single-input-single-output loops, taking advantage of the stochastic dynamics (15) which is part of the embedded model and allows any disturbance including interactions to be estimated and rejected as in (17). Attitude control is implemented around an embedded model including quaternion kinematics, Euler dynamics as in (7) and a stochastic disturbance dynamics of the same kind as (15). Coordinate decomposition (roll, pitch and yaw) is applied to the feedback design of reference generator, noise estimator and control law (Ref. 11 , 12 , 13). It relies on the assumption of small (order of milliradians) estimation and tracking errors since the early mission phases, but because of the nonlinear model in (7) it is robust against unexpected larger errors. The formation embedded model in (10) is not completely decoupled, because of interactions between altitude and distance, in the same ways as longitudinal and radial coupling in Hill's equations (Ref. 16). The FLOF angular perturbations ω_z, ω_x (yaw and roll) are decoupled from pitch as well from distance and altitude.
4) A preliminary orbit/formation control has been designed by fully decoupling (10) and applying altitude control to each satellite (Ref. 17). Full coupling will be accounted for by a next AOCS version.

D. Preliminary results and discussion

Preliminary AOCS results are shown and discussed here. They were obtained from a Matlab/Simulink simplified simulator developed by Politecnico di Torino. Some essential parts of the spacecraft are missing, like for instance thruster assembly and thruster dispatching, which is part of AOCS. Aerodynamics is rather conservative. Gravity potential includes J2 (Earth flattening). Thruster noise is missing. The orbit altitude at equator is $h = 340\text{ km}$. Eccentricity is 0.005. Accelerometer and sensor dynamics and noise are included. The orbit period is about $P_o \cong 5500\text{ s}$. Orbits are polar and pendulum formation is obtained from a RAAN (right ascension of the ascending node) offset of $\Delta\Omega \cong 2.5\text{ mrad}$ (Fig 3). The mean formation distance is $d_{nom} = 200\text{ km}$, corresponding to an anomaly offset $\Delta\nu \cong 30\text{ mrad}$ (Fig 2). Time unit of plots is ks, $100\text{ ks} \cong 1.15\text{ day}$. Notwithstanding simplifications, simulated results are indicative of the mission feasibility for what concerns the AOCS target achievements. Attitude control is actuated and aligns the control frame $\mathcal{C}_k$ to the FLOF, such that both frames can be confused in the following discussion.

All the simulated results refer to a pendulum formation with a semi-aperture of 10 degrees (the lowest limit of the range in Table 1, $\alpha_{\max} \cong 0.175\text{ rad}$) as shown in Fig 15. The left side shows the sequence of the SSL oscillations around the FLOF third axis $\vec{o}_3$ in Fig 10. The right side shows bias and drift of mean yaw (orbit average) due to drag-free residuals. Yaw formation control can only eliminate bias and drift, leaving 'natural' oscillations due to gravity.

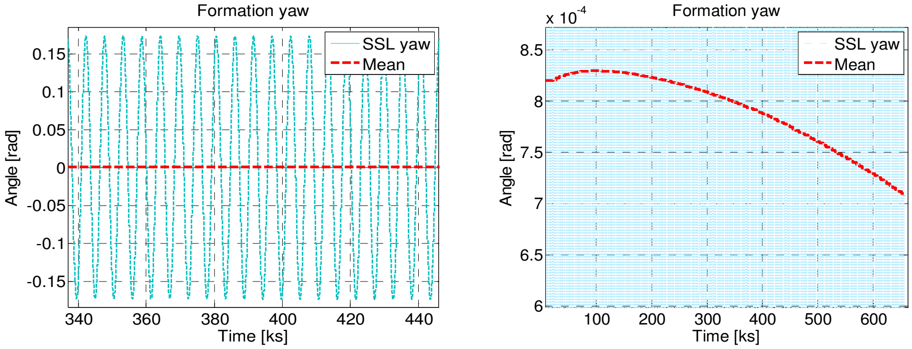

Fig 15. Formation yaw: simulated yaw angle (left), drift of the mean yaw due to drag-free residuals (right).

Unlike yaw, mean altitude and distance were under a decoupled control in the simulation run, though with a limited force authority, as shown in Fig 16 . A formation acquisition has been simulated with an initial error of about 800 m. (within the target distance fluctuation in Table 1). Distance control is actuated by the differential radial force (z axis, FLOF $\vec{o}_3$) which is computed and equally split with sign to each spacecraft. Altitude is controlled on each spacecraft by the longitudinal force (x axis, FLOF $\vec{o}_1$). The plotted variables are mean variables (averaged over the orbit period). The true distance is oscillating around the reference value.

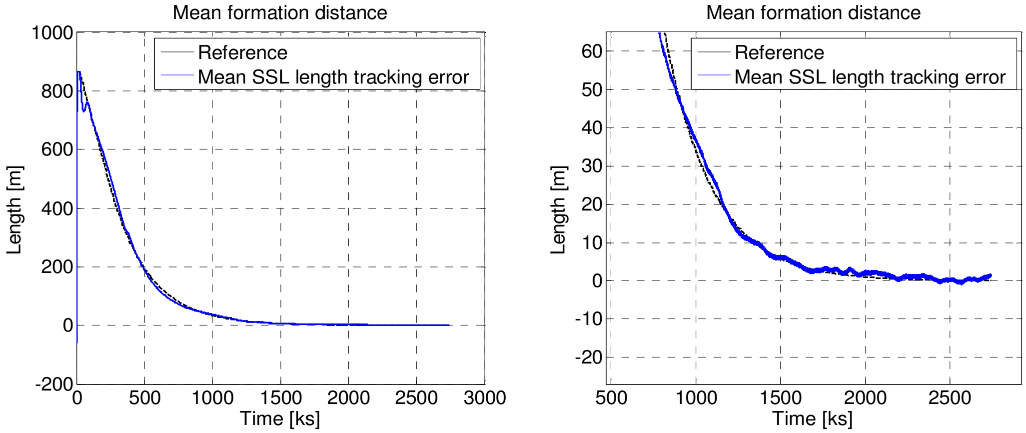

Fig 16. Distance reference and mean tracking error. Right: enlargement around zero reference.

Fig 17 shows the linear acceleration residuals (single spacecraft) which are affected by the formation acquisition (z axis). The enlargement of Fig 17 shows that the residual of the z axis is much larger than the other two axis, due to a larger bias and drift of the accelerometer z-axis. Notwithstanding this fact, the target PSD is respected as shown in Fig 18, right. One may recognize in the z-axis residual the harmonic content of the distance command, since the latter is actuated once per orbit. Distance command is saturated to 1 mN. Height control has been actuated, but no height acquisition has been simulated. The total commanded forces including drag-free, distance and altitude are in Fig 18, left. Also in the pendulum case the x axis is close to be aligned with the spacecraft speed vector (the largest misalignment being $\alpha_{\max} = 0.175 \text{ rad}$) and suffers the larger drag. Lateral drag (y axis) is mainly due to spacecraft yaw rotation (pendulum case), which aligns the first control axis $\vec{c}_{k1}$ to the SSL. The total z-axis command is not shown in Fig 18, left, being close to the distance command. The high frequency content of the spectral density in Fig 18, right, is much lower than GOCE residuals in Fig 12, since no thruster noise has been simulated. The latter is expected to be much lower than GOCE, due to a smaller size and different technology of electrical thrusters.

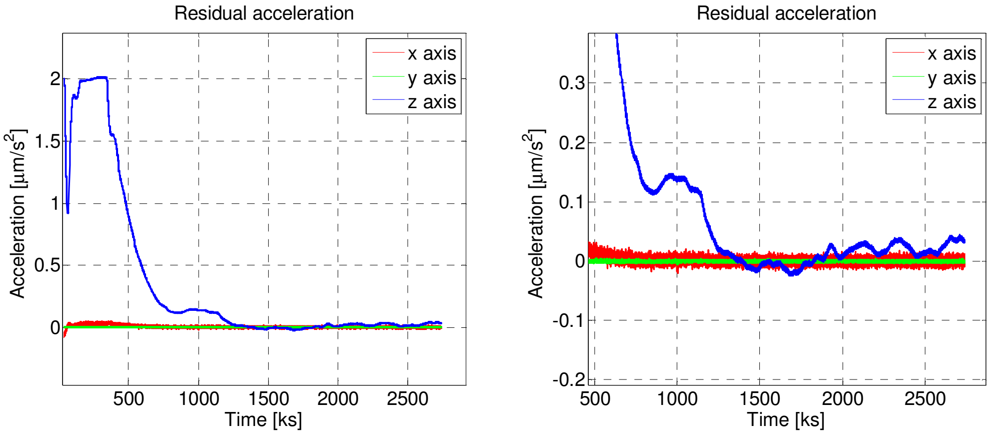

Fig 17. Residual linear acceleration. Right: enlargement around zero residual.

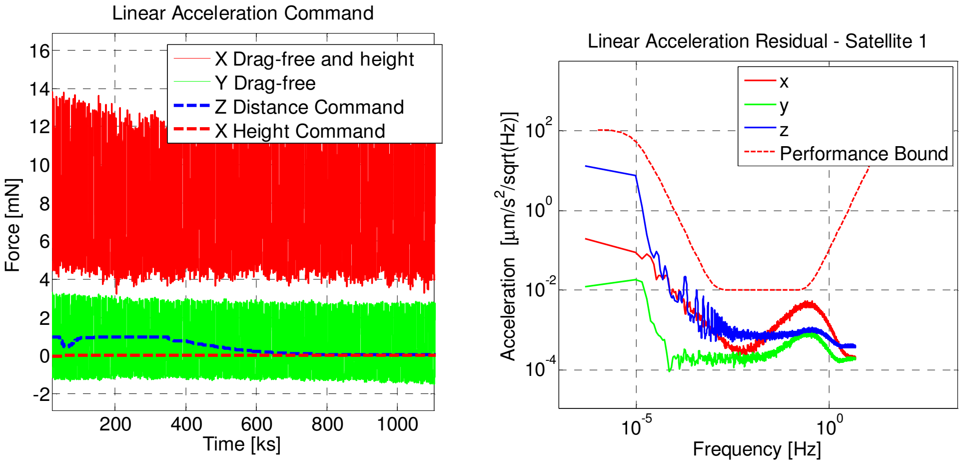

Fig 18. Left: Command forces and components. Right. Spectral density of the residual acceleration in Fig 17.

Fig 19 shows the pointing errors (pitch and yaw) of the control axis $\vec{c}_{k1}$ (corresponding to the sensor axis) with respect to the satellite-to-satellite line (the axis $\vec{o}_1$) which is materialized by the laser beam launched by the companion satellite (see Fig 11). One of the aim of the study is to compare different sensors, here indicated as sensor 1, 2 and 3. Sensor 1 and sensor 3 correspond to the telescopes in Fig 5, which are capable of providing both tilt and lateral displacement of the incoming laser beam. Sensor 3, coupled with the SSL distance, provides the pointing error of the companion satellite and must be supported by satellite interlink. Sensor 2 is an angular sensor of different technology, more accurate than sensor 1, but with a smaller field-of-view (FOV). Fig 19, left, shows the progressive attenuation of the pointing error starting from a pair of biased star trackers and proceeding through sensor 1, 2 and 3. No acquisition of the sensor FOV is simulated. Fig 19, right, compares the spectral density of the different pointing errors. The challenge is to make the sensor-2 PSD staying below the target bound (dashed line). Sensor 1 cannot respect the target bound due to expected random error. Star tracker errors do not respect the target bound, but they will be used since the early phases to progressively align control axes to FLOF, and to implement the optical sensor FOV acquisition.

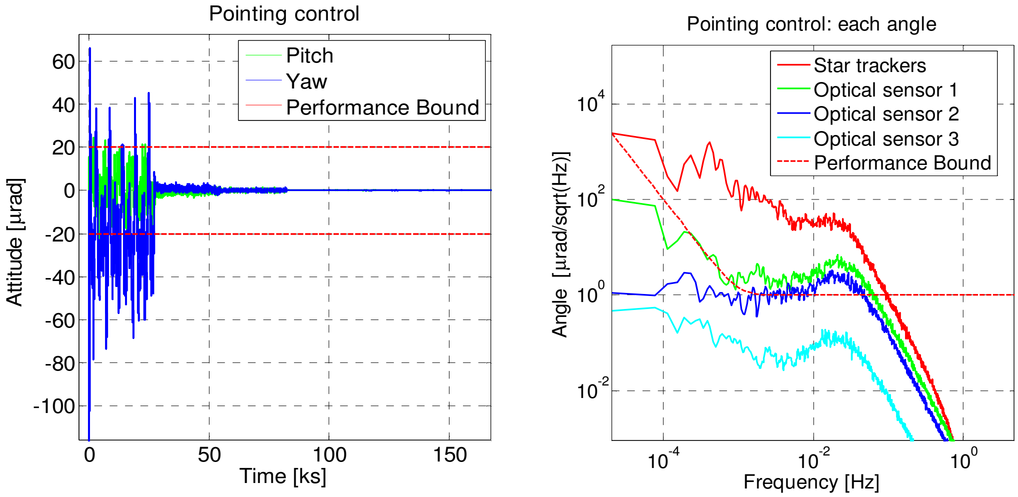

Fig 19. Pointing control. Left: time profile of the pitch and yaw angles as sensor accuracy improves. Right: spectral density for different sensors.

Fig 20 shows the angular acceleration residuals of the angular drag-free control obtained during the sensor 2 phase. At first sight the target bound is not respected below the scientific measurement band F. Since the peaks there are due to free-response (gravity forced) pendulum oscillations, they are deterministic signals not be assessed in terms of spectral density. The significant result is that attitude and drag-free control are appropriately frequency-coordinated, not to spill attitude command accelerations (the reference term in (17)) inside F.

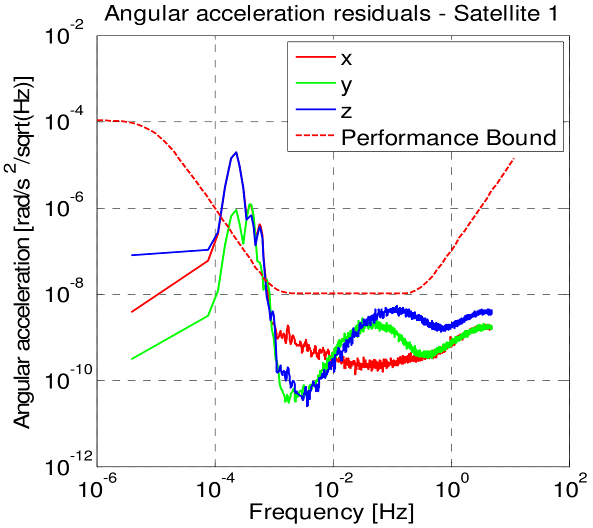

Fig 20. Residual angular acceleration during sensor 2 phase.

Acknowledgments

The material utilised to write this paper derives from the preparatory studies for the NGGM promoted and funded by the European Space Agency, and performed by Thales Alenia Space Italia with the contribution of the sub-contractors. Part of the work of the authors of Politecnico di Torino has been done under a sub-contract of the main contract awarded to Thales Alenia Space Italia.

References

1 Cesare, S., Aguirre, M., Allasio, A., Leone, B., Massotti, L., Muzi, and D., Silvestrin, P., "The measurement of Earth's gravity field after the GOCE mission", *Acta Astronautica*, Vol. 67, Numbers 7-8, October/November 2010, pp. 702–712.

2 Massotti, L., Aguirre, M., Haagmans, R., Kern, and M., Silvestrin, P., "Mission concepts overview for the preparation of ESA's next generation gravity mission", *Proceedings of the 8th International ESA Conference on Guidance, Navigation & Control Systems*, June 2011.

3 Koop, R., and Rummel, R., "The future of satellite gravimetry", *Final Report of the Future Gravity Mission Workshop*, ESA/ESTEC, Noordwijk, The Netherlands, 12–13 April 2007.

4 Bender, P.L., Wiese, D.N., and Nerem, R.S., "A Possible Dual-GRACE Mission With 90 Degree And 63 Degree Inclination Orbits", *Proceedings of the 3rd International Symposium on Formation Flying, Missions and Technologies*, Noordwijk (NL), April 2008.

5 Wiese, D. N., Nerem, R. S., and Lemoine, F. G., "Design considerations for a dedicated gravity recovery satellite mission consisting of two pairs of satellites", *Journal of Geodesy* (2012) 86:81–98.

6 Swenson, S., Wahr, J., "Post-processing removal of correlated errors in GRACE data", *Geophys. Res. Lett.*, 33, L08402, doi:10.1029/2005GL025285.

7 Cesare, S., and Pisani, M., European Patent Application for an "Interferometer", Application No. 07300862.5, filed 14 March 2007.

8 Sheard, B. S., Heinzel, G., Danzmann, K., Shaddock, D. A., Klipstein, W. M., and Folkner, W. M. "Intersatellite laser ranging instrument for the GRACE follow-on mission", Journal of Geodesy (2012) 86:1083–1095.

9 Cesare, S., and Pisani, M., European Patent Application for "Position and orientation determination", Application No. 07107090.8, filed 27 April 2007.

10 Marque, J.-P., Christophe, B., and Foulon, B., "Accelerometers of the GOCE Mission: Return of Experience from One Year of In-Orbit", *Proceedings of ESA Living Planet Symposium,* SP-686, ESA, 2010.

11 Canuto, E. "Embedded Model Control: outline of the theory", *ISA Transactions*, Vol. 46, No. 3, 2007, pp. 363-377.

12 Canuto, E., Acuna-Bravo, W., Molano-Jimenez A. and Perez-Montenegro C., "Embedded Model Control calls for disturbance modelling and rejection", *ISA Transactions*, Vol. 51, No. 5, 2012, pp. 584-595.

13 Canuto, E., Acuna-Bravo, W., and Perez-Montenegro C., "Robust control stability using the error loop", *Int. Journal of Mechatronics and Automation*, Vol. 3, No. 2, 2013, pp. 94-109.

14 Canuto E. "Drag-free and attitude control for the GOCE satellite", *Automatica,* Vol. 44, No. 7, 2008, pp. 1766-1780.

15 Canuto E., Molano-Jimenez A and Massotti L. "Drag-free control of the GOCE satellite: noise and observer design". *IEEE Trans. on Control Systems Technology*, Vol. 18, 2010, pp. 501-509.

16 Canuto E., Molano-Jimenez A., Perez-Montenegro C., Massotti L. "Long-distance, drag-free, low-thrust, LEO formation control for earth gravity monitoring". *Acta Astronautica*, Vol. 69, 2011, pp. 571-582.

17 Canuto E., Molano-Jimenez A., Buonocore M., Massotti L. and Girouart B. "Orbit and attitude control for gravimetry drag-free satellites", submitted to *Proc. of the Institution of Mechanical Engineers, Part G, Journal of Aerospace Engineering*, 2013.